

Nucleotide excision repair of 2-acetylaminofluorene- and 2-aminofluorene-(C8)-guanine adducts: molecular dynamics simulations elucidate how lesion structure and base sequence context impact repair efficiencies

Hong Mu¹, Konstantin Kropachev², Lihua Wang¹, Lu Zhang², Alexander Kolbanovskiy², Marina Kolbanovskiy², Nicholas E. Geacintov^{2,*}, and Suse Broyde^{1,*}

¹Department of Biology and ²Department of Chemistry, New York University, 100 Washington Square East, New York, NY 10003, USA

Received June 22, 2012; Revised July 24, 2012; Accepted July 26, 2012

ABSTRACT

Nucleotide excision repair (NER) efficiencies of DNA lesions can vary by orders of magnitude, for reasons that remain unclear. An example is the pair of *N*-(2'-deoxyguanosin-8-yl)-2-aminofluorene (dG-C8-AF) and *N*-(2'-deoxyguanosin-8-yl)-2-acetylaminofluorene (dG-C8-AAF) adducts that differ by a single acetyl group. The NER efficiencies in human HeLa cell extracts of these lesions are significantly different when placed at G₁, G₂ or G₃ in the duplex sequence (5'-CTCG₁G₂CG₃CCATC-3') containing the *NarI* mutational hot spot. Furthermore, the dG-C8-AAF adduct is a better substrate of NER than dG-C8-AF in all three *NarI* sequence contexts. The conformations of each of these adducts were investigated by Molecular dynamics (MD) simulation methods. In the base-displaced conformational family, the greater repair susceptibility of dG-C8-AAF in all sequences stems from steric hindrance effects of the acetyl group which significantly diminish the adduct-base stabilizing van der Waals stacking interactions relative to the dG-C8-AF case. Base sequence context effects for each adduct are caused by differences in helix untwisting and minor groove opening that are derived from the differences in stacking patterns. Overall, the greater NER efficiencies are correlated with greater extents of base sequence-dependent local untwisting and minor groove opening together with weaker stacking interactions.

INTRODUCTION

Pre-mutagenic bulky DNA lesions are subject to nucleotide excision repair (NER) that restores the integrity of genomic DNA through a 'cut and patch' mechanism (1,2). In human global genomic repair of bulky DNA lesions (3,4), the DNA damage is recognized by the NER factor XPC/Rad23B (5); subsequently, additional factors are recruited to the site of the damage, which ultimately leads to the excision of a 24–32 nt long lesion-containing oligonucleotide (6–9), followed by gap-filling DNA synthesis catalyzed by several DNA polymerases (10,11). However, the excision efficiencies of chemically different lesions by the mammalian NER apparatus vary by several orders of magnitude (1,12–14). The mechanistic origin of this phenomenon is of considerable interest particularly since lesions that escape repair can survive until replication and cause mutations which initiate cancer (15–17). A crystal structure of yeast *Saccharomyces cerevisiae* Rad4/Rad23 (18), an ortholog of the mammalian XPC/Rad23B, in complex with a DNA duplex containing a cyclobutane pyrimidine dimer (CPD), reveals that a β -hairpin is inserted into the DNA helix, separating the damaged and partner strand, and the two bases opposite the disordered CPD are flipped out of the helix and are bound to the protein. This structure supports the hypothesis that sufficient local thermodynamic destabilization plays an important role in determining lesion recognition and subsequent excision efficiency (12,19–21).

The carcinogens 2-aminofluorene (AF) and 2-acetylaminofluorene (AAF) have been studied for many decades as prototypes of the aromatic amine/amide family (22,23). The major reaction products of metabolically activated AAF and AF with guanine in DNA

*To whom correspondence should be addressed. Tel: +1 212 998 8231; Fax: +1 212 995 4015; Email: broyde@nyu.edu
Correspondence may also be addressed to Nicholas E. Geacintov. Tel: +1 212 998 8407; Fax: +1 212 998 8421; Email: ng1@nyu.edu

include the *N*-(2'-deoxyguanosin-8-yl)-2-acetylaminofluorene (dG-C8-AAF) and *N*-(2'-deoxyguanosin-8-yl)-2-aminofluorene (dG-C8-AF) adducts (Figure 1A) (24). The mutagenicity and tumorigenicity of AF and AAF have been studied extensively (22,23) and the susceptibility of their adducts to human (25–27) and prokaryotic NER (25,28–32) have also been investigated.

The relationships between the conformations of the dG-C8-AAF and dG-C8-AF adducts and their impacts on repair and translesion synthesis are of considerable interest. The structures of the dG-C8-AF and dG-C8-AAF adducts have been under investigation for many years (29,32–44). For the case of the AF adduct, two conformational themes have been defined by NMR methods in B-DNA with normal Watson–Crick base pairing (32,36–42). In one conformational family, the fluorenyl ring system is situated at the exterior of the B-DNA double helix with all Watson–Crick base pairs intact, and the damaged guanine remains in the normal B-DNA *anti* glycosidic bond conformation (36,38,40,45). A second conformational theme is base-displaced intercalation; in this case, the damaged guanine adopts the *syn* glycosidic bond conformation, the fluorenyl rings are inserted into the helix and both the adducted guanine and its partner cytosine are extruded into the major groove (41,45). These two conformational families are in equilibrium in normally paired DNA duplexes; the adjacent and even next-nearest neighbor base sequence contexts determine the population balance (37,38). Additionally, there is NMR evidence for conformational interchange in the orientation of the fluorenyl ring system showing that it may rotate $\sim 180^\circ$ about its long axis

(40,41) (rotation about β' ; Figure 1A). A third conformational family was also determined from high resolution NMR studies in which the adducted guanine is *syn* and the fluorenyl ring system is wedged into the B-DNA minor groove for the case of G–A (46,47) and G–I (48) mismatch structures. These structural families have been extensively characterized by CD, fluorescence, F^{19} NMR and differential scanning calorimetry (29,33). NMR data have also provided a model for the dG-C8-AAF adduct in the single CG*C sequence context; this work showed a base-displaced intercalated conformation for $\sim 70\%$ of the population, but the other conformations remained structurally undefined (35). Recently, the Cho laboratory has revisited the complex conformational properties of the dG-C8-AAF adduct, and the mix of conformations and its sequence dependence were determined in detail using F^{19} NMR methods. These studies have demonstrated that the dG-C8-AAF adduct can assume three different types of conformations, namely, major groove, base-displaced intercalated and minor groove Wedge, and that the fractional populations of each state are strongly sequence-dependent (32,34). The existence of both the Wedge and the major groove conformers had been predicted previously on the basis of computational analysis of these structures (49,50).

The sequence 5'-CTCG₁G₂CG₃CCATC-3', which includes the *NarI* restriction site in the center (underlined), contains an *Escherichia coli* -2 deletion mutational hot spot at G₃ (51–53) that is manifested in translesion synthesis of dG-C8-AAF adducts (51). The -2 deletion activity is dependent on the activity of DNA Pol II (53) and a recent crystal structure of DNA Pol II provides a

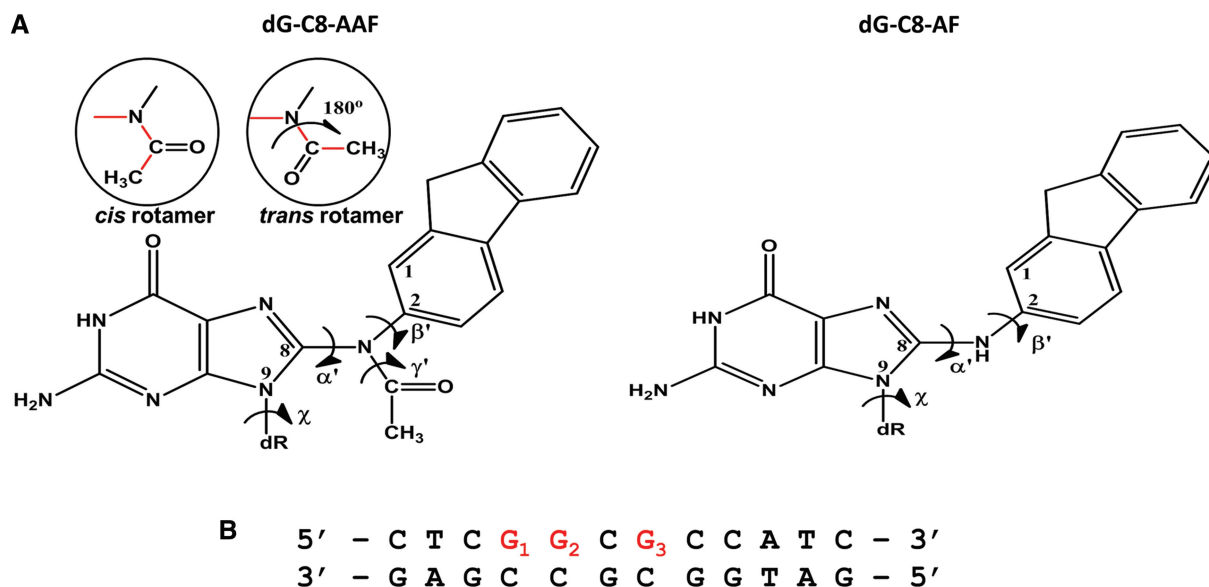


Figure 1. Chemical structures of the adducts and 12-mer sequence of lesion containing duplexes used in the experiments. (A) Chemical structures of dG-C8-AAF and dG-C8-AF. Torsion angles at the linkage site are defined as follows: α' , N9 (G*)–C8 (G*)–N–C2; β' , C8 (G*)–N–C2–C1; γ' , C8 (G*)–N–C–C (methyl); glycosidic torsion of damaged guanine, χ , O4'–C1'–N9–C4. *cis* ($\gamma' = 0^\circ$) and *trans* ($\gamma' = 180^\circ$) rotamers of the acetyl group are shown in the circles. (B) *NarI*-hotspot-containing 12-mer duplex used in the NER experiments. G₁, G₂ and G₃ in the duplex denote the guanine that is damaged by dG-C8-AAF or dG-C8-AF. Simulated 9-mer sequences are 5'-ACTCG*GCGC-3' for the G₁*; 5'-CTCGG*CGCC-3' for the G₂* and 5'-CGGCG*CCAT-3' for the G₃* duplex (Supplementary Table S1), so that G*, the damaged guanine, is at the center of the simulated 9-mer in each case.

structural explanation (54). Furthermore, human cell free extracts were also recently shown to produce -2 deletions induced by the dG-C8-AAF adduct at G₃ in the *NarI* sequence and these were partially dependent on pol η (55). The solution structures of both dG-C8-AF and dG-C8-AAF adducts have also been investigated by NMR methods with modification at positions G₁, G₂ and G₃ of the *NarI* sequence (Figure 1B) and the relative proportions of the three types of adduct conformations described above have been evaluated at each guanine (32,34). Hence, this is an excellent model system for investigating the effects of adduct structure, conformation and base sequence context on NER susceptibility.

In this study we determined the relative excision efficiencies of both the dG-C8-AF and the dG-C8-AAF adducts in the *NarI* sequence context with the adducts positioned at either G₁, G₂ or G₃ (Figure 1B) in human HeLa cell extracts. Molecular dynamics (MD) simulations, based on known NMR solution structures (35,40,41,49,50), were utilized to analyze the structural and dynamic features of each of these adducts in the three *NarI* sequence contexts. The objectives of this study were to elucidate how these lesions perturb the local double-helical DNA structure and to determine whether the structural perturbations can be correlated with observed differences in NER efficiencies. Our analyses provide a structural explanation for the experimentally observed differences in NER efficiencies between the dG-C8-AAF and dG-C8-AF adducts, and show how the NER dual incision efficiencies of each lesion depend on the identities of adjacent base pairs at the G₁, G₂, and G₃ positions in the *NarI* sequence.

MATERIALS AND METHODS

Synthesis and separation of oligonucleotides with *NarI*-G₁*AAF, *NarI*-G₂*AAF and *NarI*-G₃*AAF adducts

The 5'-CTCGGCGCCATC-3' 12-mer sequence was reacted with excess of *N*-acetoxy-2-acetylaminofluorene (AAF) in 2 mM sodium citrate buffer as described (56). Briefly, the three mono-adducted [AAF]-modified oligonucleotides were isolated from the reaction mixture using reversed phase HPLC methods. The first separation was carried out using a linear 5–40% acetonitrile (ACN)/50 mM triethylammonium acetate (TEAA, pH 7.0) buffer solution gradient using a semi-preparative PRP-1 column (7.0 × 250 mm, Hamilton Company). The second and third separations were carried out using a linear 10–24% ACN/50 mM TEAA (pH 7.0) buffer solution gradient. The position of the modified guanine base in each of the three mono-adducted oligonucleotides was determined by a sequencing method that involves the partial exonuclease digestion method described in detail by Kolbanovskiy *et al.* (57). Briefly, in this method, the exonuclease digestion is arrested at the site of the lesion and the masses of the exonuclease-resistant fragments are determined by MALDI TOF mass spectrometry, thus establishing the positions of the lesions.

After separation and purification, the pure [AAF]-modified oligonucleotides were converted to the

deacetylated AF-modified oligonucleotides by treatment of the solutions with 1 M NaOH containing 0.3% (v/v) 2-mercaptoethanol for 45 min at room temperature, followed by separation of the sequence-isomeric oligonucleotides and their purification using reversed phase HPLC and C18 ODS-Hypersil columns with a linear 12–30% ACN/50 mM TEAA (pH 7.0) buffer solution gradient.

The purified oligonucleotides containing the single dG-C8-AF or dG-C8-AAF adduct were ³²P-5'-end-labeled and incorporated into 135-mer oligonucleotide duplexes by standard ligation methods and then added to NER-competent cell extracts, as described in detail by Kropachev *et al.* (58). In all cases, the lesions were positioned at the 67th nucleotide counted from the 5' side. Supplementary Figure S1 shows the 135-mer sequences and other experimentally relevant supplementary data are given in Supplementary Figures S2 and S3.

Human NER assays in HeLa cell extracts

The NER assays were conducted as described earlier by Kropachev *et al.* (58). In brief, each reaction contained 1 pmol of P³²-internally labeled 135-mer duplex with an adduct at the 67th nucleotide counted from the 5'-side in an aqueous mixture generated by mixing 17.5 μ l of a 1 M KCl solution with 20 μ l of a 10 mM Tris-ATP (pH 7.9) and 10 μ l freshly prepared cell extract solution containing 40–45 μ g of protein, and sufficient dialysis buffer (12 mM MgCl₂, 25 mM Hepes-KOH pH 7.9, 2.5 mM Dithiothreitol, 1 mM EDTA 10% glycerol) to produce a final volume of 50 μ l. After appropriate incubation time and subsequent preparation of the samples (58), the reaction products were loaded onto a 12% polyacrylamide, 8 M urea denaturing gel. The gels were dried, exposed and analyzed using a Storm 840 phosphorimager and Image-Quant software.

MD simulations

In order to obtain molecular explanations for the experimental findings, we carried out extensive MD simulations. We investigated all structural families that have been experimentally observed by NMR methods for dG-C8-AF and dG-C8-AAF-modified duplexes (35,40,41) and studied each structural family at each of the guanines, G₁, G₂ and G₃ (Figure 1B), of the *NarI* sequence context. The lesions were embedded in duplex 9-mers with the damaged guanine centrally positioned in each case. The families for dG-C8-AF are: major groove and base-displaced intercalated, and for dG-C8-AAF: major groove, base-displaced intercalated and minor groove Wedge. We did not include the Wedge conformation for dG-C8-AF since this conformation has been observed only in duplexes containing mismatches opposite the damaged guanine (46–48). We also investigated for the dG-C8-AF case the rotamers about the long axis of the fluorenyl moiety (governed by the torsion angle β' , Figure 1A), where such rotamers had been observed experimentally for the base-displaced and major groove conformational families (37). The initial models were constructed based on NMR solution structures for all

cases except for the dG-C8-AAF major groove and Wedge conformers, which were obtained by modeling (49,50); we added the acetyl group (*cis* rotamer, Figure 1A) to the dG-C8-AF major groove and Wedge NMR structures (37), and replaced the mismatched partner A to the modified guanine (G*) with a C for the Wedge. Figure 2 shows the central 5-mers of these structures for the G₂* duplex. Supplementary Table S1 summarizes all 21 simulations for the modified duplexes. An unmodified control (5'-CTCGGCGCCA-3') was also studied. MD simulations of all structures with explicit water and counterions were carried out for 50 ns using the AMBER9 simulation package (59). Full details of the molecular modeling, force fields (Supplementary Table S2) and MD protocols are given in the Supplementary Materials and Methods. All simulations achieved good stability after 20.0 ns (Supplementary Figure S4). Structural ensembles from 20.0 ns to 50.0 ns were employed for analyses, except for analyses for the β' torsion angle of all dG-C8-AF-modified duplexes, for which the first 20 ns was retained to preserve the initial state following equilibration to investigate the possibility of rotation during the simulations (Supplementary Figure S5). The PTRAJ module of AMBER 9 (59) and AMBER 10 (60), the CARNAL module of AMBER 7 (61) and the Curves+ software package (62) were employed for structure and energy analyses. Details of the analyses are provided in the Supplementary Materials and Methods. PyMOL (Delano Scientific, LLC) (63) was employed to make molecular images and movies.

RESULTS

Nucleotide excision repair assays

The incubation of 135-mer G₁*, G₂* and G₃* duplexes containing single dG-C8-AF and dG-C8-AAF lesions in HeLa cell extracts gives rise to the appearance of radioactively labeled oligonucleotide dual incision fragments 24–32 nt in length. The 10R (+)-*cis-anti*-B[a]P-N²-dG

lesion, also embedded at the 67th nucleotide in the 135-mer duplexes, is an excellent NER substrate (64,65) and was used as a positive control of NER activity (Figure 3A). Comparisons of the relative extents of NER were calculated from the integration of the radioactivity in the 25–32 oligonucleotide dual excision fragment region divided by the total radioactivity in each lane of the gel autoradiogram; a typical example of such a gel is shown in Figure 3A. The results with all seven modified oligonucleotide substrates were performed with one and the same cell extract. The base line radioactivity signals were subtracted when the NER efficiencies were low as in the case of the dG-C8-AF-modified G₂* duplexes. In order to achieve satisfactory reproducibility from day-to-day, and to take into account the varying activities of different cell extracts prepared at different times, the NER efficiencies in each gel autoradiogram were normalized to the value obtained with the 10R (+)-*cis-anti*-B[a]P-N²-dG-modified 135-mer duplex after an incubation time of 45 min. These NER efficiencies were arbitrarily assigned a value of 100 and all other NER efficiencies are reported relative to this value. The dual incision kinetics, determined from the fractions of the 24–32 nt long dual incision fragments excised from the 135-mer duplexes, are depicted in Figure 3B and C. Each value is the average of six independent experiments relative to the dual incision efficiency obtained at the 45 min time points with the 10R (+)-*cis-anti*-B[a]P-N²-dG-modified 135-mer duplexes; the actual NER efficiency at this time point for this *cis*-lesion was $6.2 \pm 2.3\%$ (average of six experiments). The linear time dependence of dual incision products suggests that the NER efficiency is not limited by the availability of NER proteins that cooperate in generating the dual incision efficiencies. Using similar substrates with G*CG* intrastrand cisplatin-derived cross-linked lesions which are better NER substrates (dual incision product yields in the range of ~10%) than the lesions of interest in this work, we find that the yields of incision products are also proportional to the damaged DNA substrate concentration (data not shown). Overall, these observations are

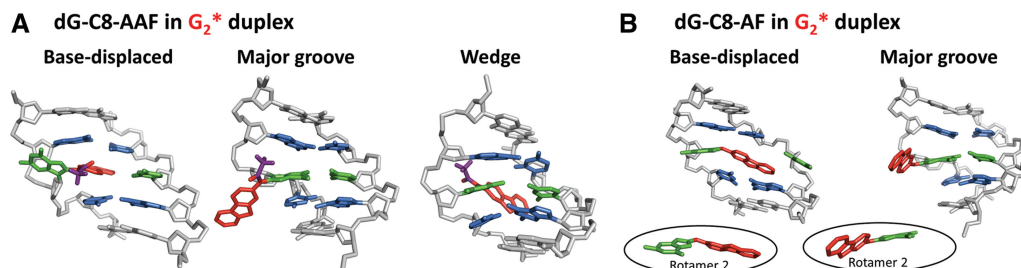


Figure 2. Generic structural features of conformational families in dG-C8-AAF and dG-C8-AF-modified duplexes. Shown are the initial structures for MD simulations for dG-C8-AAF and dG-C8-AF-modified G₂* duplexes. Central 5-mers of the structures are viewed from the major groove side. (A) Base-displaced, major groove and Wedge conformers of the dG-C8-AAF-modified G₂* duplex. (B) Base-displaced and major groove conformers of dG-C8-AF-modified G₂* duplex. The β' rotamer 1 for each of the base-displaced and major groove conformers is illustrated. The G* and the fluorenyl rings of the β' rotamer 2 are shown in the circles at the bottom. These rotamers represent the rotation along the long axis of the fluorenyl rings. The β' values of Rotamer 1 and Rotamer 2 are given in Supplementary Table S1. The most representative structures from the MD ensembles are shown in Figures 7, 9, 10, Supplementary Figures S6, S12 and S14. All structures are represented in sticks: hydrogen and phosphate oxygen atoms are deleted for clarity, except for the hydrogen atoms of the acetyl groups. The lesion-containing strands and the complementary strands are in light gray. The fluorenyl rings are red, the acetyl group of AAF is purple and the acetyl oxygen is red. The modified guanines and partner C bases are green, and the neighboring bases are blue. In the nomenclature of the Cho laboratory, the major groove conformation is designated 'B', the base-displaced intercalated conformation is designated 'S' and the Wedge conformation is designated 'W' (32).

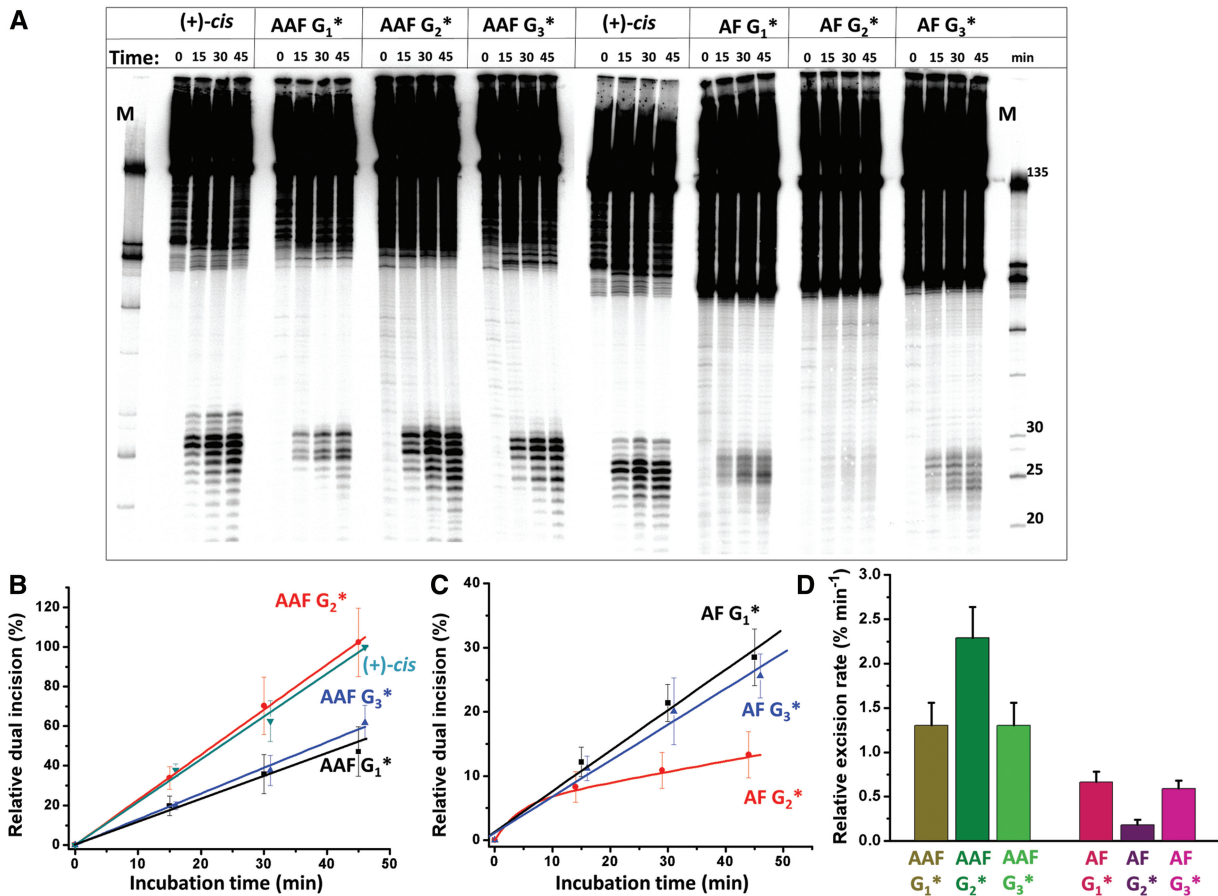


Figure 3. Nucleotide excision repair of dG-C8-AAF and dG-C8-AF lesions incorporated at either G_1 , G_2 , or G_3 in the 12-mer *NarI* sequences embedded in the center of 135-mer duplexes as a function of incubation time in extracts from human HeLa cells. (A) Autoradiograph of representative denaturing (8 M urea) 12% polyacrylamide gel. The 10R (+)-*cis-anti-B[a]P-N²-dG* adduct [(+)-*cis*] in the 5'-CCATCG*CTACC-3' sequence context was included in these experiments as a positive control (58) and as a measure of the variable NER activities of different cell extracts (see text). The lanes marked 'M' show the mobilities of oligonucleotide length markers. The exact sequence of the 135-mer is shown in Supplementary Figure S1. Time dependence of fractions of dual incision products in the 20–30 nt long oligonucleotide range as a function of incubation time for (B) dG-C8-AAF G_1^* , G_2^* and G_3^* duplexes and (C) dG-C8-AF G_1^* , G_2^* and G_3^* duplexes. Inverted triangles (cyan): (+)-*cis*-adducts; squares (black): modified G_1^* duplexes; circles (red): modified G_2^* duplexes; triangle (blue): modified G_3^* duplexes. The individual data points are averages of six independent experiments normalized with respect to the control DNA substrates, expressed as a percent of the dual incision result obtained with the (+)-*cis* adducts at the 45 min time point in each experiment and assigned an arbitrary value of 100%; the actual measured NER efficiencies at this time point were in the range of ~3–9% with an average of 6.2% expressed in terms of (radioactivity in the 20–30 nt range)/(total radioactivity)×100. The straight lines represent the least-squares fits to the data points. (D) Relative rates of dual incisions estimated from the slopes of the straight lines in (B) and (C). In the case of the dG-C8-AF-modified G_2^* duplex substrate, only the relative rate of the slower component (~92–96% of the sample) is shown; a faster, minor component is incised within the first 15 min and its rate was not further characterized.

consistent with the notion that the differences in NER efficiencies observed (Figure 3) are associated with a recognition step in the multi-step NER process that is rate limiting (7,14,66,67). Most recently, the work of Luijsterburg *et al.* (67) showed that lesion recognition is strongly rate limiting for mammalian NER in living cells based on extensive kinetic measurements of binding and dissociation of individual components of the NER machinery utilizing live cell imaging.

When the fractions of dual incision products increase linearly with incubation time and the best straight line drawn through the data points intercepts the vertical axis at the zero point, either a homogeneous adduct population, or a conformationally heterogeneous population with overall indistinguishable NER efficiencies is indicated. However, if the best straight line intercepts

the vertical axis with an apparent NER efficiency greater than zero, a conformational heterogeneity of adducts with different NER efficiencies is indicated. In the case of the dG-C8-AAF-modified G_1^* , G_2^* , G_3^* and the 10R (+)-*cis-anti-B[a]P-N²-dG*-modified duplexes, the time dependence of dual incision product formation is linear (Figure 3B). In the case of the dG-C8-AF-modified G_1^* and G_3^* duplexes, the best least squares fit is also linear, although the straight lines calculated are close to but do not exactly intersect the vertical axis at the zero-point (Figure 3C). However, the time-dependence of product formation is strongly non-linear in the case of the dG-C8-AF G_2^* duplex; this is clearly evident from the non-zero vertical axis intercept of the best straight line drawn through the experimental data points. This suggests that the dG-C8-AF G_2^* duplex, while

structurally homogeneous, is conformationally heterogeneous. The non-linearity suggests that this substrate contains two or more conformationally different dG-C8-AF G₂* duplex structures, which are characterized by markedly different NER efficiencies. The vertical axis intercept of the dG-C8-AF G₂* sample is ~5% which is approximately equal to the more rapidly repaired fraction, while the major fraction is the most slowly repaired among all of the lesions observable in the experiments.

The initial rates of dual incisions are compared in the bar graph in Figure 3D. Overall, there is a difference by a factor of ~13 for the best (dG-C8-AAF G₂*) and the worst (dG-C8-AF G₂*) NER substrates. The dual incision rates are the same for the dG-C8-AAF G₂* and the 10R (+)-*cis-anti*-B[a]P-N²-dG modified DNA duplexes within experimental error. The relative NER rates for the dG-C8-AAF G₁* and dG-C8-AAF G₃* duplexes are the same within experimental error as well and are about 1.8 times smaller than the dG-C8-AAF G₂* rates. It is noteworthy that our results for the dG-C8-AAF adduct with HeLa cell extracts follow the same trend as those obtained earlier by Mu *et al.* (25), with the dG-C8-AAF G₂* duplex being repaired significantly more efficiently than the dG-C8-AAF G₁* and dG-C8-AAF G₃* duplexes. Thermal melting studies (Supplementary Figure S2) also show that the dG-C8-AAF adducts destabilize double-stranded DNA more extensively than the dG-C8-AF adducts as has been observed previously (33,68). The NER rates are uniformly lower for all dG-C8-AF adducts than for all three dG-C8-AAF adducts, and are similar in value for the dG-C8-AF-modified G₁* and G₃* duplexes. The NER efficiencies of these duplexes are a factor of ~3.5 greater than the major fraction (95%) of the dG-C8-AF-modified G₂* duplex, which is the least readily repaired one.

Molecular modeling and MD simulations

In order to provide molecular explanations for the experimental NER results, we carried out MD simulations for duplexes containing the dG-C8-AF and dG-C8-AAF adducts at the G₁, G₂ and G₃ positions of the *NarI* sequence (Figure 1B) that were studied experimentally. For the dG-C8-AF adduct, we simulated the base-displaced intercalated and major groove conformers, including rotamers of β' (Figure 2) that were experimentally observed (37). For the dG-C8-AAF adduct, we simulated these two conformations and also the minor groove Wedge conformer, as these are the conformers observed for each adduct by F¹⁹ NMR in normally Watson-Crick base paired duplexes (32,34,35,37,38). We also simulated an unmodified control duplex. Supplementary Table S1 summarizes our 21 simulations. We carried out detailed analyses of the MD trajectories between 20 and 50 ns, during which the simulations were stable, as shown by the RMSD data of each 50 ns MD simulation (Supplementary Figure S4).

Earlier results have shown that bulky polycyclic aromatic B[a]P-derived DNA lesions with base-displaced intercalated conformations (e.g. the 10R (+)-*cis-anti*-B[a]P-N²-dG lesion employed as a control in the above

experiments) are better substrates of NER than those positioned in the minor groove (26) or those with classical intercalative conformations without base displacement (69,70). Other examples of base-displaced intercalated adducts that are also excellent substrates of NER are the dG-C8-AAF (12,25), the *N*-(deoxyguanosin-8-yl)-2-amino-1-methyl-6-phenylimidazo[4,5-*b*]pyridine (dG-C8-PhIP), (71) and the *N*-(deoxyguanosin-8-yl)-1-aminopyrene (dG-C8-AP) adducts (72). In order to further establish the validity of this paradigm, we analyzed the structural and energetic features of all the conformational families of the dG-C8-AF and dG-C8-AAF adducts in all three *NarI* sequence contexts (base-displaced and major groove for dG-C8-AF, and base-displaced, major groove and minor groove Wedge for dG-C8-AAF). We found that the base-displaced conformers induce the most prominent structural and energetic distortions in the modified DNA duplexes, namely ruptured Watson-Crick hydrogen bonding, stacking destabilization, untwisting and minor groove enlargement which are all hallmarks of DNA lesions that are good substrates of NER (21,69).

The following sections describe the specific structural distortions of the different conformational families depicted in Figure 2. The results reveal that the base-displaced intercalated DNA lesions are the most extensively distorted, and that the distortions correlate with relative repair susceptibilities of dG-C8-AAF and dG-C8-AF and their respective sequence context dependence. By contrast, the major groove and Wedge conformations are shown to be much less distorted.

The major groove and Wedge conformational families are little distorted compared with the unmodified control

As shown in Figure 4, for both dG-C8-AAF and dG-C8-AF-modified duplexes, the major groove conformers retain normal B-DNA Watson-Crick base pairing and strong van der Waals stacking interactions that are comparable to the unmodified control. Furthermore, for dG-C8-AAF-modified duplexes, the Wedge conformers also have close to normal stacking (Figure 4), and one strong non-Watson-Crick hydrogen bond between the G* and partner C, as well as a second weaker one in two of the three sequences (Supplementary Figures S6, S7 and Supplementary Table S3). Furthermore, as shown in Figure 5, the helical twist and minor groove dimensions of these major groove and Wedge conformers (Supplementary Figures S8, S9 and Supplementary Tables S4, S5) are much closer to normal than for the base-displaced ones as discussed below.

Higher repair susceptibility of dG-C8-AAF than dG-C8-AF adducts in their base-displaced intercalated conformations is correlated with weaker stacking interactions accompanied by more untwisting and minor groove enlargement

Significantly weaker stacking interactions in the base-displaced dG-C8-AAF duplexes

The importance of perturbations of the normal DNA base stacking interactions by DNA lesions, such as one

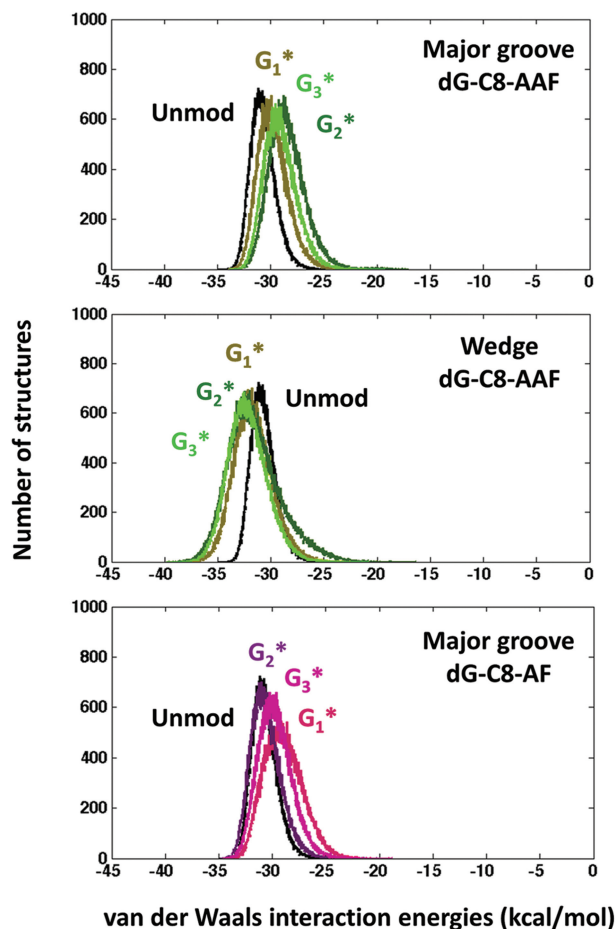


Figure 4. Stabilizing local van der Waals stacking interaction energies of the major groove and Wedge conformers are comparable to the unmodified control. For the major groove conformers, the van der Waals interaction energy between the lesion base pair and its neighboring base pairs are computed. For the Wedge conformers, the stacking interaction energy also includes the interaction between the fluorenyl rings and the DNA backbone residues in contact with it in the minor groove (detailed in Supplementary Materials and Methods). For the unmodified control, the mean trimer value over all three sequences is shown for clarity, since the individual values of the three sequences are very similar (Supplementary Table S5). The mean values and standard deviations of the block averages (Supplementary Materials and Methods) for the stacking interaction energies of the major groove and Wedge conformers are given in Supplementary Table S4.

containing a crosslink between guanine and thymine in DNA duplexes (73), as well as the potential stabilizing effects associated with interactions between aromatic rings of carcinogens with DNA bases has been considered recently (69,71,74); evidence was presented that weakened van der Waals stacking interactions correlate with enhanced NER susceptibility whereas enhanced stacking interactions result in diminished excision efficiencies. Accordingly, we evaluated the van der Waals stacking interaction energies for all simulated base-displaced structures. These energies are 10–13 kcal/mol less stabilizing for the base-displaced dG-C8-AAF duplexes than for the dG-C8-AF duplexes (Figure 6 and Supplementary Table S6).

The origin of the large difference in stacking energies between the dG-C8-AF and dG-C8-AAF adducts is due

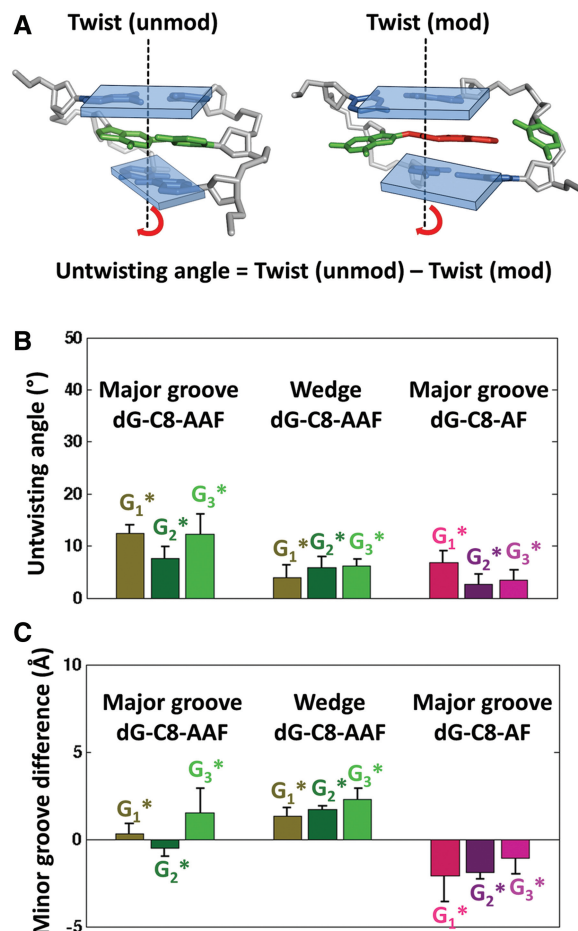


Figure 5. The structural features of twist and minor groove width in the Major groove and Wedge conformers of the modified duplexes are close to the normal values of the unmodified duplex. (A) Definition of helical untwisting in modified duplexes. The twist angles of the modified duplexes [Twist (mod)] are between the two base pairs surrounding the G*, and represent the local impact on helix twisting imposed by the adduct. The twist angle of the unmodified control [Twist (unmod)] is the average of the two-step twist angles of the CGG, GGC and CGC trimers, but all are very similar (Supplementary Table S5). The unmodified and modified trimers are rendered as in Figure 2. Helical axes are shown as black dashed lines, and the base pair planes as transparent rectangular plates. (B) Untwisting angle values of the major groove and Wedge conformers. The untwisting angles are computed as in (A). The mean values and standard deviations of the block averages (Supplementary Materials and Methods) for the untwisting angles are shown. (C) Differences between minor groove widths of modified duplexes and unmodified control for major groove and Wedge conformers. Minor groove difference = Minor groove width_{modified} – Minor groove width_{unmodified}. For the modified duplexes the minor groove width is measured at the lesion site between P7–P16 and for the unmodified control the minor groove width is measured at analogous positions (Supplementary Figure S9). The mean values and standard deviations of the block averages (Supplementary Materials and Methods) for the minor groove differences are shown.

to the acetyl group in the latter adduct. Although the fluorenyl rings intercalate into the helix and stack with neighboring base pairs in both the dG-C8-AAF and dG-C8-AF base-displaced duplexes, the modified guanines are positioned differently. In the dG-C8-AAF case, the modified guanine G* is displaced into the

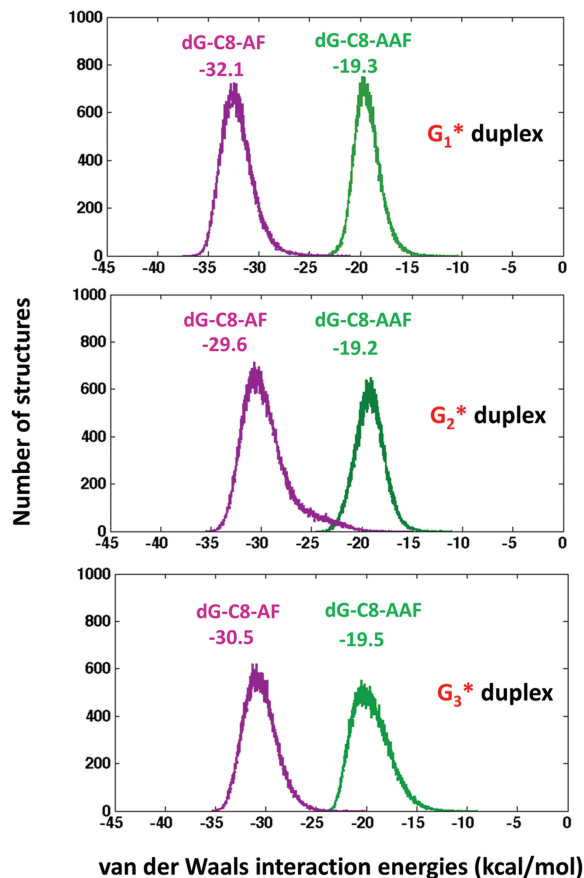


Figure 6. Stacking stabilization is much stronger for dG-C8-AF than dG-C8-AAF in the base-displaced duplexes. Shown are the population distributions with mean values of the van der Waals stacking interaction energies between lesion and adjacent bases in base-displaced dG-C8-AAF and dG-C8-AF duplexes. For the dG-C8-AF duplexes, the lesion guanine, G*, is included (Supplementary Materials and Methods) to account for its stacking with adjacent bases. These results are for the β' rotamer 1; similar results were obtained for β' rotamer 2 (Figure 2B and Supplementary Table S6).

major groove (Figure 7A) and is aligned nearly perpendicularly to the fluorenyl rings. This alignment is dictated by steric restraints posed by the acetyl group and facilitates G* forming two hydrogen bonds with the backbone (Figure 7A, Supplementary Table S3). In this position, the G* is in close steric contact with its own deoxyribose residue whose orientation therefore becomes distorted so that it is perpendicular to the helix axis rather than in the normal parallel position (Figure 7A and Supplementary Movie S1) and its sugar pucker oscillates between different conformations (Supplementary Figure S10A). However, in the dG-C8-AF case, without the acetyl group, the displaced G* is closer to being co-planar with the fluorenyl rings and is partly stacked with its 5' neighboring base on the same strand (Figure 7B and Supplementary Movie S2); its sugar residue is oriented normally with stable puckering (Supplementary Figure S10B). Thus, the modified guanine base G* provides additional stacking stabilization and, being unrestrained, also allows the fluorenyl rings to reach further across to the complementary strand, which also improves the stacking interactions. The G*/fluorenyl ring orientational difference in dG-C8-AAF

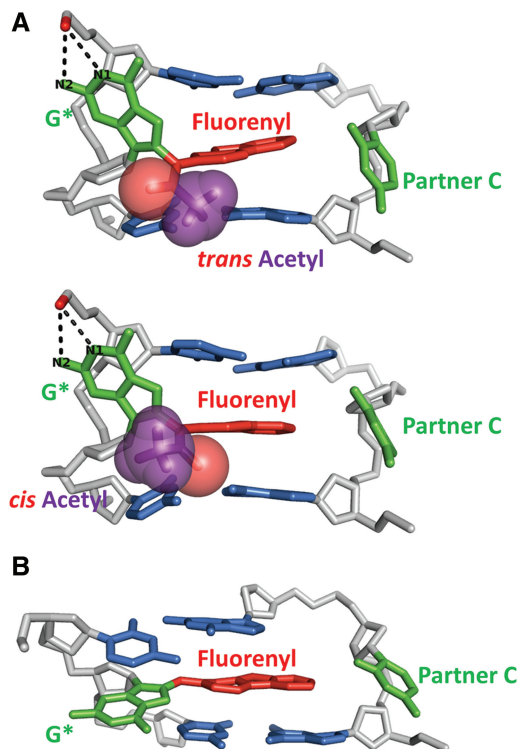


Figure 7. The acetyl group imposes a different base-displaced intercalated conformation in dG-C8-AAF than in dG-C8-AF. Note the different positions of G*. For illustration the G₃* duplexes are presented. (A) Most representative structures of dG-C8-AAF-modified G₃* duplex with acetyl group in *cis* and *trans* conformation (Figure 1). G₃* was selected for this illustration because both *cis* and *trans* rotamers of the acetyl group were observed in the simulations (see Supplementary Results). Stereo views are available in Supplementary Figure S14. See also Supplementary Movies S1 and S3. (B). Most representative structure of dG-C8-AF-modified G₃* duplex. For both adducts, the G₁* and G₂* duplexes have overall similar intercalation structures as in the G₃* duplex. See also Supplementary Movie S2. The central trimers are viewed from the major groove side and represented as in Figure 2, except that the phosphate oxygen that forms hydrogen bonds with G* is shown in red stick. The hydrogen bonds between G* and backbone phosphate oxygen are represented using black dashed lines. The acetyl group is shown in transparent CPK (purple and red).

and dG-C8-AF is shown in crystal structures containing G-AAF (75,76) and base-displaced dG-C8-AF (77), as well as in the high resolution NMR structures of dG-C8-AF adducts in double-stranded DNA (37).

Greater untwisting and minor groove enlargement in base-displaced dG-C8-AAF duplexes

Untwisting and minor groove enlargement may contribute to distortions and destabilizations that can facilitate NER (21). Untwisting at the lesion site is reflected in a decrease of the twist angle, relative to the unmodified control, between the 5' and 3' base pairs that are adjacent to the lesion (Figure 5A). The smaller the twist angle, the more untwisted the duplex. We note that intercalation is always associated with helix untwisting (78,79), the extent of which depends on the structure of the intercalated moiety (69). For the dG-C8-AAF and dG-C8-AF adducts, the backbone untwists so that the base pairs adjacent to the lesion are optimally stacked with the elongated fluorenyl moiety. However, the untwisting in

the dG-C8-AAF modified duplexes is always greater than for the dG-C8-AF adducts (Figure 8A and B) (the difference is sequence dependent, as discussed further below). This greater untwisting relative to the unmodified duplex in the dG-C8-AAF case results from the steric restraints imposed by the acetyl group (Figure 7A and Supplementary Movie S1), which impedes the free adjustment of the backbone twist. In each case, the untwisting is accompanied by minor groove enlargement, which is also greater for dG-C8-AAF in all sequences (Figure 8C). The correlation of these properties is shown in Supplementary Figure S11.

Sequence-dependence of stacking patterns in base-displaced intercalated conformations produce differences in untwisting and minor groove opening that correlate with the base sequence dependence of NER dual incision efficiencies

The G₂ sequence is the best repaired for dG-C8-AAF*

The experimental results showed that G₂* is incised roughly twice as efficiently as G₁* or G₃* (Figure 3D). All show homogenous initial repair rates (Figure 3B). In order to gain insights into this sequence effect, we analyzed the sequence dependence in structural properties of the dG-C8-AAF duplexes manifested in our dynamics simulations. The governing feature is the sequence dependence of stacking patterns between the fluorenyl ring system and adjacent base pairs.

In the dG-C8-AAF adducts, stacking is restricted by steric effects associated with the acetyl group, which prevents stacking interactions between the modified guanine G* and adjacent bases and inhibits the ability of the fluorenyl ring system to move closer to the opposite strand (Figure 7A). In the G₁* duplex, the optimal stacking pattern involves the stacking of the fluorenyl rings with the cytosine on the 5' side of G* and the partner strand cytosine on the 3' side (Figure 9A and Supplementary Figure S12A). In the G₂* duplex, optimal interactions are achieved by the stacking of the fluorenyl rings with the guanine on its 5' side and the partner strand guanine on its 3' side (Figure 9B and Supplementary Figure S12B). In the G₃* case, optimal stacking involves overlap of the fluorenyl rings with the cytosine on the 5' side of G* and the six membered ring of the partner strand guanine on the 3' side (Figure 9C and Supplementary Figure S12C). The *cis/trans* conformational possibilities of the acetyl group (Figures 1A and 7A) play a role in modulating optimal stacking in each of the three *NarI* sequence-containing duplexes. Details are given in Supplementary Figures S13–S14 and Movie S3.

Achieving the optimal stacking interactions in each sequence requires different adjustments in untwisting as well as different minor groove enlargements. The G₂* duplex is characterized by the greatest untwisting (i.e. it exhibits the lowest twist angle between the base pairs surrounding the intercalated fluorenyl rings) (Figures 8B and 9B), whereas the degree of untwisting is significantly lower as well as similar in the G₁* and G₃* duplexes (Figures 8B, 9A and C). Compared with the analogous

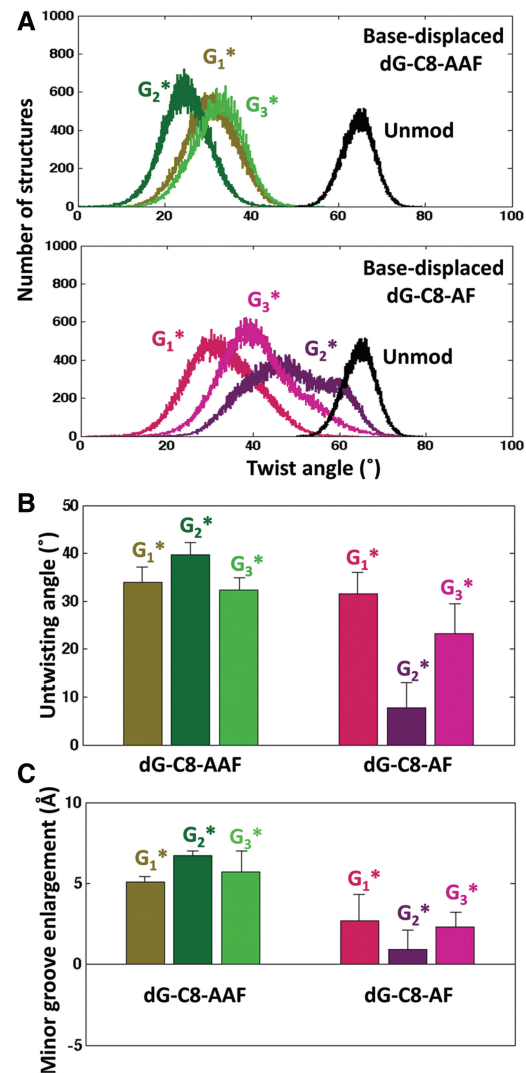


Figure 8. The extent of untwisting and minor groove enlargement for the base-displaced conformations is greatest for dG-C8-AAF at G₂* and least for the proposed slowly repaired population of dG-C8-AF at G₂*. (A) Population distributions of twist angles for the base-displaced conformers and that of the unmodified control. (B) Untwisting angles for the base-displaced conformers. The untwisting angle is calculated as in Figure 5B. The mean values and standard deviations of the block averages (Supplementary Materials and Methods) for the untwisting angles are shown. (C) Minor groove enlargement of the base-displaced conformers. Minor groove enlargement = Minor groove width_{modified} – Minor groove width_{unmodified}. The minor groove widths are measured as in Figure 5C. The mean values and standard deviations of the block averages (Supplementary Materials and Methods) for the minor groove differences are shown. For dG-C8-AF at G₂*, standard deviations are for all structures of the less untwisted population (Supplementary Figure S16).

twist angle of the unmodified control (Figure 9D), all three sequences are significantly untwisted. In each case, untwisting is accompanied by concomitant minor groove enlargement, the extent of which follows the order of untwisting angles (Figure 8B and C; Supplementary Table S6). The differences in these distorting features are correlated with the sequence dependence of the relative NER susceptibilities, with the most untwisting and

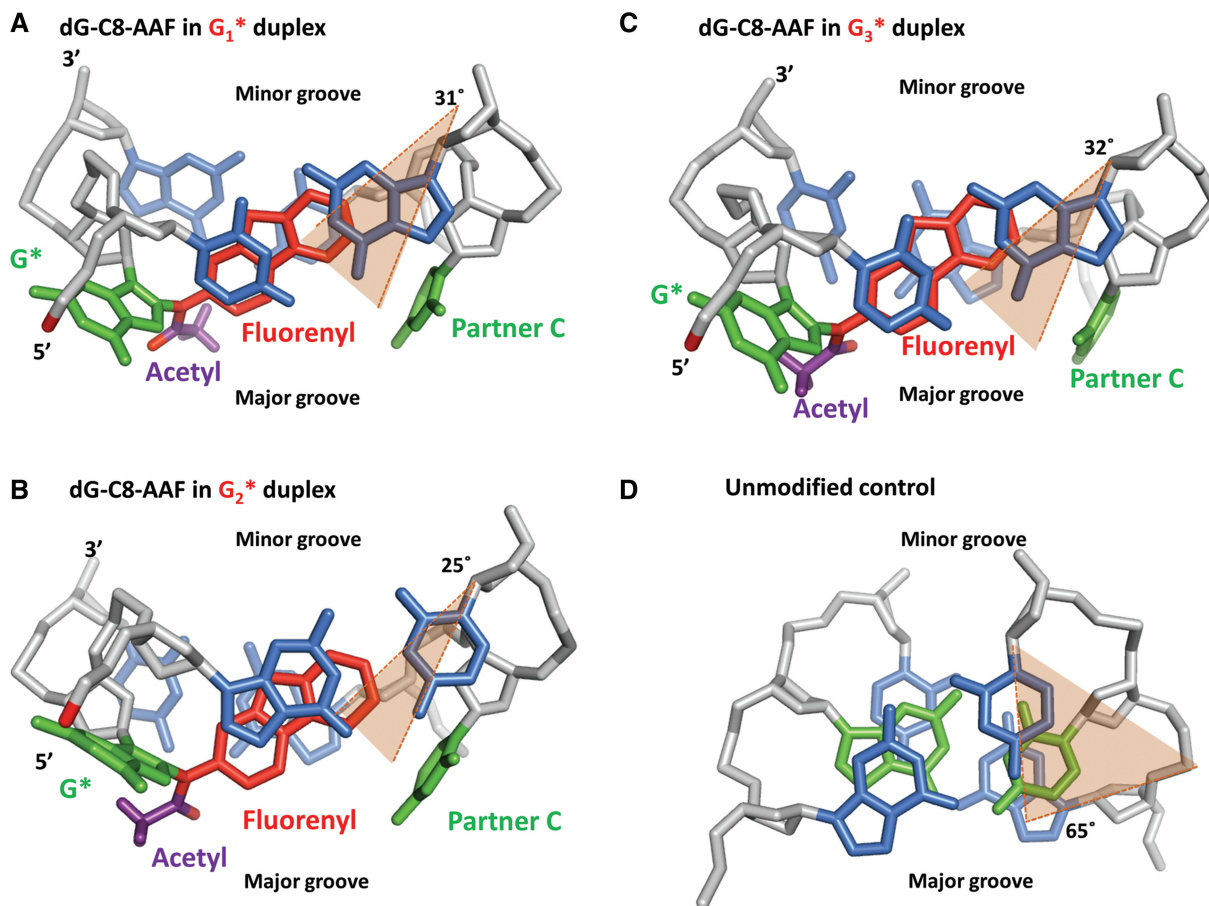


Figure 9. Views along the helix axis reveal sequence-dependent differences in stacking patterns of the base-displaced dG-C8-AAF-modified duplexes. The stacking pattern differences determine the extent of untwisting. Central trimers of the most representative structures are shown. (A) dG-C8-AAF-modified G₁* duplex. (B) dG-C8-AAF-modified G₂* duplex. (C) dG-C8-AAF-modified G₃* duplex. (D) Twist angle of the unmodified control in the representative 5'-GGC-3' trimer. Other trimer sequences are similar in twist angle (Supplementary Table S5). The twist angle between the 5' and 3' base pairs is shown in orange shade with the mean value of the twist angle for each population labeled. The greater the twist angle, the less the untwisting relative to the unmodified duplex. The modified structures are rendered as in Figure 7A without CPK. The unmodified control is rendered as in Figure 2. Stereo views are shown in Supplementary Figure S12.

greatest minor groove opening occurring at the most repaired dG-C8-AAF lesion, at G₂* (Figure 3D). In accord with the homogenous repair rates, the population distributions of twist angles manifest homogenous populations for all three duplexes (Figure 8A).

The dG-C8-AAF adduct at G₂* exhibits a short rapidly repaired phase and a predominant slowly repaired phase

The experimental NER results reveal that heterogeneity is manifested to a significant extent only in the case of the dG-C8-AAF adduct at G₂* (Figure 3C). Moreover, the dual incision efficiency of G₂* in its dominant phase is about one-third that of G₁* and G₃*, which are repaired with approximately equal efficiencies (Figure 3D). Interestingly, the two repair phases are consistent with a heterogeneous population distribution of twist angles between the base pairs 5' and 3' to the lesion, observed only in the case of the dG-C8-AAF adduct at G₂*, but not at G₁* and G₃* (Figure 8A).

With the same dG-C8-AAF adduct positioned at G₁* and G₃*, the distributions for the twist angles revealed a homogenous population for each case (Figure 8A). The

most representative adduct structures for the G₁* and G₃* duplexes are shown in Figure 10A and B. In the dG-C8-AAF-modified G₁* duplex, the base 5' to the G* is a C; this C stacks very weakly with the modified guanine; hence the fluorenyl ring system is free to adjust its position to maximize stacking interactions with the partner strand bases, allowing strong overlap between the fluorenyl rings and the 3'-C and 5'-G partner strand bases (Figure 10A). This stacking pattern results in significant untwisting of the G₁* duplex (Figure 8B), accompanied by minor groove opening (Figure 8C). In the case of the G₃* duplex, the G* stacks only partially with its 5' side C on the same strand, and the fluorenyl rings can thus optimize stacking interactions with the partner strand bases: the fluorenyl moiety achieves extensive stacking with the 5' G, as well as a perfect one ring overlap with the 3' G in the partner strand (Figure 10B). This stacking pattern produces untwisting and minor groove opening of the dG-C8-AAF-modified G₃* duplex quite close to that of the analogous G₁* duplex (Figure 8B and C).

The two distinct twist angle populations observed only in the case of the dG-C8-AAF-G₂* duplex are characterized by

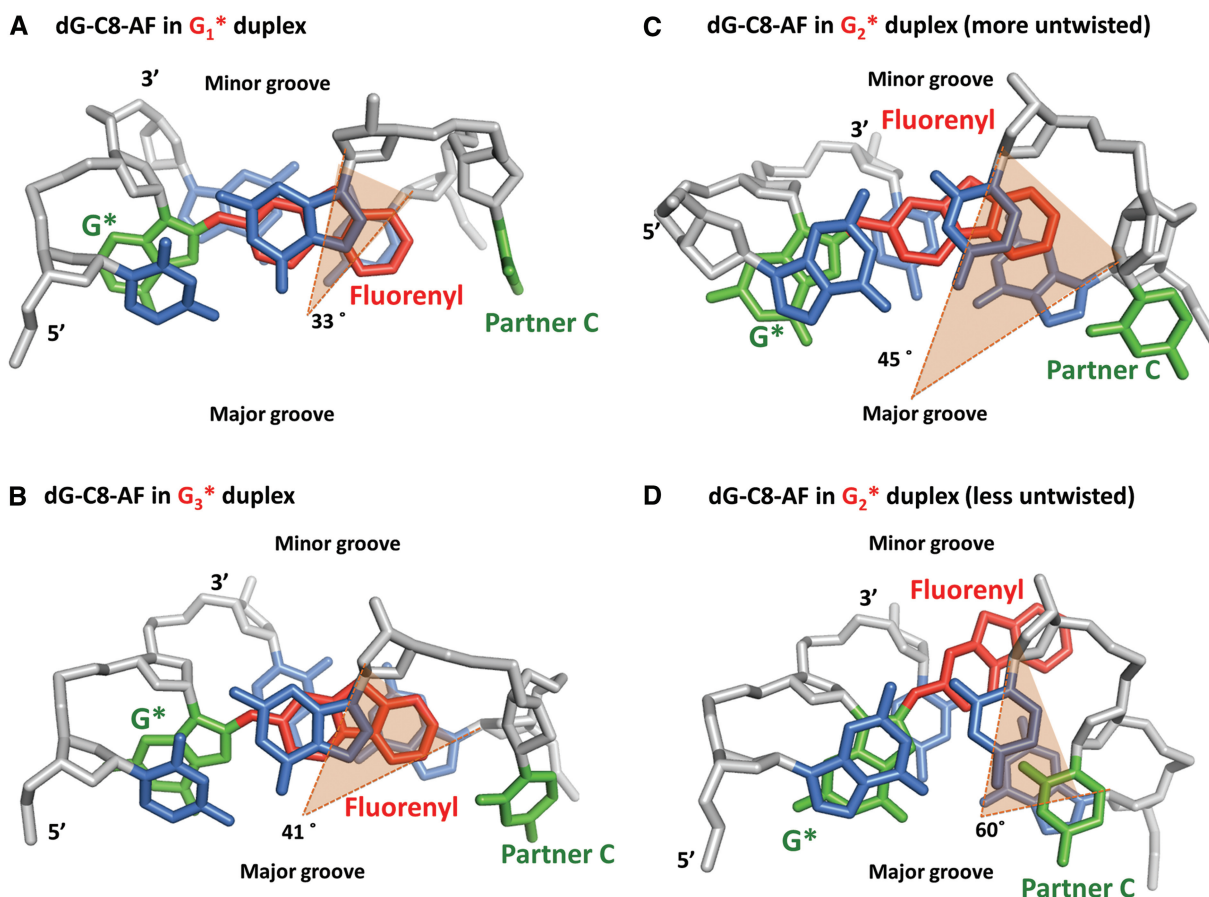


Figure 10. Views along the helix axis reveal sequence-dependent differences in stacking patterns of the base-displaced dG-C8-AF-modified duplexes. The stacking pattern differences determine the extent of untwisting. Central trimers of the most representative structures are shown. (A) dG-C8-AF-modified G_1^* duplex. (B) dG-C8-AF-modified G_3^* duplex. (C) The more untwisted population of dG-C8-AF-modified G_2^* duplex. (D) The less untwisted population of dG-C8-AF-modified G_2^* duplex. The structures are rendered as in Figure 2. The twist angles between the 5' and 3' base pairs are represented as in Figure 9.

a more untwisted population with a mean twist angle value of $\sim 45^\circ$ and a second much less untwisted one with a mean twist angle value of $\sim 60^\circ$ (Figure 10C and D; Supplementary Figure S16). These two populations display different extents of protrusion of the fluorenyl rings into the minor groove. Figure 10C and D shows representative structures of each of these twist populations, illustrating the different positions of the fluorenyl rings. In the population with twist angle of $\sim 60^\circ$, the modified guanine and its 5'-G are well stacked, at the expense of poorer stacking by the fluorenyl rings, which extend further into the minor groove (Figure 10D). The population with twist angle of $\sim 45^\circ$ has weaker stacking between the modified guanine and its 5'-G and well-stacked fluorenyl rings (Figure 10C); it resembles the structures of the G_1^* and G_3^* duplexes in Figure 10A and B. However, the $\sim 60^\circ$ twist angle population is only modestly untwisted ($\sim 5^\circ$, Figure 8B) with the lowest minor groove enlargement (Figure 8C). We hypothesize that this modestly untwisted base-displaced conformer is the slowly repaired one for the dG-C8-AF-modified G_2^* duplex; the rapid repair phase can then be attributed to the more untwisted population which resembles the G_1^* and G_3^* duplexes (Figure 10). Figures 3D, 8B and C show

how the greater NER susceptibilities correlate with greater untwisting angles and minor groove enlargements. The extent of untwisting also impacts the position of the displaced partner C: the more untwisted the structure the greater the displacement. Details are given in Supplementary Figure S17 and Supplementary Table S7.

Populations in the MD simulations with extrusion of the fluorenyl rings into the minor groove suggest a pathway for rotation about the fluorenyl long axis in the base-displaced intercalated dG-C8-AF duplex

NMR studies have shown two populations of rotamers representing a flip about the fluorenyl long axis and governed by the β' torsion angle for base-displaced dG-C8-AF adducts (37). Our MD simulations for the G_2^* duplex have suggested a possible pathway for this reorientation involving fluorenyl ring protrusion into the minor groove, detailed in Supplementary Data (Supplementary Figures S16, S18 and Supplementary Movie S4).

DISCUSSION

Our analyses of the base-displaced intercalated and major groove conformations of the dG-C8-AF adducts, and the

base-displaced intercalated, major groove and minor groove Wedge conformations for the dG-C8-AAF adducts (Figure 2) suggest that extensive distortions and destabilizations in the base-displaced intercalated adducts are correlated with the relative NER susceptibilities of dG-C8-AAF and dG-C8-AF and their sequence dependence. The major groove and Wedge conformations are less distorted and thus are suggested to be less susceptible to NER (Figures 5 and 8). These findings support our hypothesis that the base-displaced intercalated conformation is the more repair susceptible one. Our experiments with both dG-C8-AF and dG-C8-AAF adducts do not allow the general interpretation that the solution population of the base-displaced conformation (Supplementary Table S8) correlates with the relative repair susceptibility in our human NER assay. This is reasonable since solution population balances determined by NMR are temperature sensitive in the 1–25°C range (33,41), may differ in the presence of the repair machinery, and the machinery can respond differently to the same adduct in prokaryotic and eukaryotic systems (25,28,32), discussed in detail in Liu *et al.* (80).

A notable feature of the NER experiments is the much greater excision efficiency of the dG-C8-AAF compared with the dG-C8-AF adduct, irrespective of sequence context. This has been observed previously in prokaryotic systems (28,29,31–33,77). In the case of eukaryotic NER, there is only one early report describing the relative NER efficiencies of dG-C8-AAF but not dG-C8-AF adducts in the *NarI* sequence, and the sequence dependence was not explained (25). Our relative NER efficiencies of dG-C8-AAF adducts in the *NarI* sequence context are in good agreement with those of Mu *et al.* (25). In addition, the Schärer laboratory (Yeo, J.E., Khoo, A., Fagbemi, A.F., Schärer, O.D., submitted for publication) have recently investigated the NER efficiencies of dG-C8-AAF and dG-C8-AF lesions in the *NarI* sequence context embedded in a plasmid, albeit with different sequences flanking the *NarI* sequence. The focus of the Yeo *et al.* study was on correlating the NER efficiencies with the thermodynamic destabilizations induced by the lesions and the binding affinities of XPC/Rad23B to the modified sequences. The overall NER efficiencies and general conclusions were similar to those reported here; a single difference (relative NER efficiencies exhibited in the case of dG-C8-AAF at G₂* and G₃*) may be attributed to differences in the use of linear versus circular DNA substrates or, perhaps, to the differences in the *NarI* flanking sequences. Additional details are given in Supplementary Figure S3. Interestingly, the sequence-dependent mutagenicity of dG-C8-AF and dG-C8-AAF in mammalian Chinese Hamster Ovary cells at G₁, G₂ and G₃ of the *NarI* sequence (81) is inversely correlated with the NER efficiencies observed here; this suggests that the structures determine both the repair susceptibility and the mutagenicity of the lesions, consistent with the concept that lesions that escape repair can survive to replication and cause mutations (15–17).

Our analyses showed that both the dG-C8-AAF and dG-C8-AF adducts in their base-displaced conformations exhibit ruptured Watson–Crick base pairing, local

untwisting and minor groove opening. However, the dG-C8-AAF adduct has weaker stacking interactions than the dG-C8-AF adduct; the weaker stacking is accompanied by greater untwisting and minor groove opening, which stems from the steric effect of the acetyl group. The AAF acetyl group restrains the modified guanine base G* in the major groove and only the fluorenyl aromatic ring system is intercalated (Figure 7A and Supplementary Movie S1). However, in the case of the dG-C8-AF adduct, the fluorenyl rings are intercalated and the modified guanine can partially stack with an adjacent 5' base (Figure 7B and Supplementary Movie S2). Crystallographic and NMR data support these structural differences (37,75–77). The greater NER excision efficiency of dG-C8-AAF relative to the dG-C8-AF adduct is explained by the lower van der Waals stacking stabilization provided by the intercalating lesion, greater untwisting and greater minor groove opening.

The observed sequence dependence of NER efficiencies results from sequence-governed differences in stacking patterns which produce differences in the extents of untwisting and minor groove opening. The greatest repair susceptibility observed with the dG-C8-AAF adduct is at G₂*; in this case, the fluorenyl rings are stacked with neighboring guanine bases on the 5' side of G₂* on its own strand and on the 3' side of G₂* on the complementary strand (Figure 9B). This particular fluorenyl ring/base stacking pattern produces the most untwisted adduct conformation of all three dG-C8-AAF adduct-containing duplexes, with the greatest minor groove opening; these structural perturbations are associated with the greatest NER efficiency among all of the six adducts investigated here (Figure 3). In the case of dG-C8-AF, the lowest repair susceptibility for the dominant slowly repaired phase of the three modified duplexes is observed with the modification at G₂*. Without the acetyl group, the modified guanine can stack well with the guanine on its 5' side, causing the fluorenyl aromatic rings to protrude into the minor groove in the base-displaced conformer proposed to represent the slowly repaired phase (Figure 10D); this conformer has the least untwisting and minor groove opening of all six duplexes (Figure 8B and C). Thus, these weakest structural perturbations are correlated with the lowest efficiency of NER observed among the six duplexes studied (Figure 3). Furthermore, the heterogeneity in repair rates and twist angle populations observed only for this modified duplex among the six investigated results from a combination of effects: the absence of the acetyl group's steric restraint and the presence of the 5'G base only in the G₂* sequence; together they permit stabilization of the less untwisted population only for the dG-C8-AF-modified G₂* duplex (Figure 10). We note that severe untwisting with minor groove enlargement is a structural feature of the damaged duplex in the Rad4/Rad23 crystal structure (18), suggesting that these distortions could aid in facilitating lesion recognition.

Finally, it is worth mentioning that simulations, such as in the current NMR-based work, have the advantage of providing molecular structures of individual conformers, where solution populations are heterogeneous; in this

case, biophysical data such as thermal melting cannot deconvolute the contributions of the individual conformational states. Hence, the simulations can provide molecular insights on both biophysical and biochemical experiments that are otherwise elusive.

CONCLUSION

The present experimental and computational studies with dG-C8-AF and dG-C8-AAF adducts in the *NarI* sequence context support the hypothesis that sufficient local thermodynamic destabilization can facilitate the recognition step that leads to the excision of these lesions (18–20). It is generally accepted that the recognition step is rate-determining in eukaryotic NER (7,14,66,67), and our approach of correlating NER efficiencies to the structural features of lesions in double-stranded DNA is based on this concept, although the impact of downstream effects on excision efficiencies cannot be excluded (21,80). The local thermodynamic impact of a lesion results from a net balance between lesion-induced destabilizing distortions and stabilizing van der Waals interactions between the lesion aromatic ring systems and neighboring base pairs in intercalated conformations (69,71). The much greater stacking stabilization of the dG-C8-AF adduct compared with dG-C8-AAF, combined with its less distorting impact on helix untwisting and minor groove enlargement, explain the significantly lower susceptibility to the nucleotide excision repair of the dG-C8-AF adducts. The sequence-dependent NER efficiencies on the other hand, stem from differences in DNA structural distortions caused by the lesions that include untwisting and minor groove enlargement; they stem from sequence-governed differences in stacking patterns. The present study highlights the important role played by lesion structure and base sequence context in determining NER excision efficiencies (21,69,82). Furthermore, it demonstrates how MD simulations can deconvolute certain properties of individual conformers in heterogeneous populations, which may be difficult to elucidate experimentally.

SUPPLEMENTARY DATA

Supplementary Data are available at NAR Online: Supplementary Tables 1–8, Supplementary Figures 1–18, Supplementary Movies 1–4, Supplementary Materials and Methods, Supplementary Results and Supplementary References [32,35,37,40,41,49,50,59,61,62,83–97].

ACKNOWLEDGEMENTS

In this work we used the computational resources of the Extreme Science and Engineering Discovery Environment (XSEDE), which is supported by the National Science Foundation (NSF) and the multi-purpose high performance computing resource of New York University (NYU-ITS). The content is solely the responsibility of the authors and does not necessarily represent the

official views of the National Cancer Institute or the National Institutes of Health.

FUNDING

National Institutes of Health (NIH) [CA-099194 to N.E.G., CA-75449 to S.B.]; Computational infrastructure and systems management [R01CA28038 to S.B., in part]; Components of this work were conducted in the Shared Instrumentation Facility at NYU that was constructed with support from a Research Facilities Improvement Grant [C06 RR-16572]; National Center for Research Resources, NIH; The acquisition of the MALDI-TOF mass spectrometer used in this work was supported by the National Science Foundation [CHE-0958457]. Funding for open access charge: NIH [CA-75449 to S.B.].

Conflict of interest statement. None declared.

REFERENCES

- Gillet, L.C. and Schäfer, O.D. (2006) Molecular mechanisms of mammalian global genome nucleotide excision repair. *Chem. Rev.*, **106**, 253–276.
- Hanawalt, P.C. and Spivak, G. (2008) Transcription-coupled DNA repair: two decades of progress and surprises. *Nat. Rev. Mol. Cell Biol.*, **9**, 958–970.
- Rechkunova, N.I. and Lavrik, O.I. (2010) Nucleotide excision repair in higher eukaryotes: mechanism of primary damage recognition in global genome repair. *Subcell. Biochem.*, **50**, 251–277.
- Nouspikel, T. (2009) DNA repair in mammalian cells: nucleotide excision repair—variations on versatility. *Cell. Mol. Life Sci.*, **66**, 994–1009.
- Mocquet, V., Laine, J.P., Riedl, T., Yajin, Z., Lee, M.Y. and Egly, J.M. (2008) Sequential recruitment of the repair factors during NER: the role of XPG in initiating the resynthesis step. *EMBO J.*, **27**, 155–167.
- Schäfer, O.D. and Campbell, A.J. (2010) Mechanisms of base excision repair and nucleotide excision repair. In: Geacintov, N.E. and Broyde, S. (eds), *The Chemical Biology of DNA Damage*. Wiley-VCH, Weinheim, Germany, pp. 239–260.
- Sugasawa, K., Okamoto, T., Shimizu, Y., Masutani, C., Iwai, S. and Hanaoka, F. (2001) A multistep damage recognition mechanism for global genomic nucleotide excision repair. *Genes Dev.*, **15**, 507–521.
- Evans, E., Fellows, J., Coffey, A. and Wood, R.D. (1997) Open complex formation around a lesion during nucleotide excision repair provides a structure for cleavage by human XPG protein. *EMBO J.*, **16**, 625–638.
- Riedl, T., Hanaoka, F. and Egly, J.M. (2003) The comings and goings of nucleotide excision repair factors on damaged DNA. *EMBO J.*, **22**, 5293–5303.
- Overmeer, R.M., Gourdin, A.M., Giglia-Mari, A., Kool, H., Houtsmuller, A.B., Siegal, G., Fouteri, M.I., Mullenders, L.H. and Vermeulen, W. (2010) Replication factor C recruits DNA polymerase delta to sites of nucleotide excision repair but is not required for PCNA recruitment. *Mol. Cell. Bio.*, **30**, 4828–4839.
- Ogi, T., Limsirichaikul, S., Overmeer, R.M., Volker, M., Takenaka, K., Cloney, R., Nakazawa, Y., Niimi, A., Miki, Y., Jaspers, N.G. *et al.* (2010) Three DNA polymerases, recruited by different mechanisms, carry out NER repair synthesis in human cells. *Mol. Cell.*, **37**, 714–727.
- Gunz, D., Hess, M.T. and Naegeli, H. (1996) Recognition of DNA adducts by human nucleotide excision repair. Evidence for a thermodynamic probing mechanism. *J. Biol. Chem.*, **271**, 25089–25098.
- Wood, R.D. (1999) DNA damage recognition during nucleotide excision repair in mammalian cells. *Biochimie*, **81**, 39–44.

14. Sugasawa, K., Shimizu, Y., Iwai, S. and Hanaoka, F. (2002) A molecular mechanism for DNA damage recognition by the xeroderma pigmentosum group C protein complex. *DNA Repair (Amst.)*, **1**, 95–107.
15. Henkler, F., Stolpmann, K. and Luch, A. (2012) Exposure to polycyclic aromatic hydrocarbons: bulky DNA adducts and cellular responses. In: Luch, A. (ed.), *Molecular, Clinical and Environmental Toxicology*. Springer Basel AG, Basel, Switzerland, pp. 107–131.
16. Phillips, D.H. and Arlt, V.M. (2009) Genotoxicity: damage to DNA and its consequences. *EXS*, **99**, 87–110.
17. Clapp, R.W., Jacobs, M.M. and Loechler, E.L. (2008) Environmental and occupational causes of cancer: new evidence 2005–2007. *Rev. Environ. Health*, **23**, 1–37.
18. Min, J.H. and Pavletich, N.P. (2007) Recognition of DNA damage by the Rad4 nucleotide excision repair protein. *Nature*, **449**, 570–575.
19. Geacintov, N.E., Broyde, S., Buterin, T., Naegeli, H., Wu, M., Yan, S. and Patel, D.J. (2002) Thermodynamic and structural factors in the removal of bulky DNA adducts by the nucleotide excision repair machinery. *Biopolymers*, **65**, 202–210.
20. Schäfer, O.D. (2007) Achieving broad substrate specificity in damage recognition by binding accessible nondamaged DNA. *Mol. Cell*, **28**, 184–186.
21. Cai, Y., Patel, D.J., Broyde, S. and Geacintov, N.E. (2010) Base sequence context effects on nucleotide excision repair. *J. Nucleic Acids*, **2010**, Article ID 174252; 9 pages, doi:10.4061/2010/174252.
22. Heflich, R.H. and Neft, R.E. (1994) Genetic toxicity of 2-acetylaminofluorene, 2-aminofluorene and some of their metabolites and model metabolites. *Mutat. Res.*, **318**, 73–114.
23. Kriek, E. (1992) Fifty years of research on *N*-acetyl-2-aminofluorene, one of the most versatile compounds in experimental cancer research. *J. Cancer Res. Clin. Oncol.*, **118**, 481–489.
24. Beland, F.A. and Kadlubar, F.F. (1985) Formation and persistence of arylamine DNA adducts *in vivo*. *Environ. Health Perspect.*, **62**, 19–30.
25. Mu, D., Bertrand-Burggraf, E., Huang, J.C., Fuchs, R.P., Sancar, A. and Fuchs, B.P. (1994) Human and *E. coli* excinucleases are affected differently by the sequence context of acetylaminofluorene-guanine adduct. *Nucleic Acids Res.*, **22**, 4869–4871.
26. Hess, M.T., Gunz, D., Luneva, N., Geacintov, N.E. and Naegeli, H. (1997) Base pair conformation-dependent excision of benzo[*a*]pyrene diol epoxide-guanine adducts by human nucleotide excision repair enzymes. *Mol. Cell. Biol.*, **17**, 7069–7076.
27. Gillet, L.C., Alzeer, J. and Schäfer, O.D. (2005) Site-specific incorporation of *N*-(deoxyguanosin-8-yl)-2-acetylaminofluorene (dG-AAF) into oligonucleotides using modified ‘ultra-mild’ DNA synthesis. *Nucleic Acids Res.*, **33**, 1961–1969.
28. Seeberg, E. and Fuchs, R.P. (1990) Acetylaminofluorene bound to different guanines of the sequence -GGCGCC- is excised with different efficiencies by the UvrABC excision nuclease in a pattern not correlated to the potency of mutation induction. *Proc. Natl Acad. Sci. USA*, **87**, 191–194.
29. Meneni, S.R., Shell, S.M., Gao, L., Jurecka, P., Lee, W., Spomer, J., Zou, Y., Chiarelli, M.P. and Cho, B.P. (2007) Spectroscopic and theoretical insights into sequence effects of aminofluorene-induced conformational heterogeneity and nucleotide excision repair. *Biochemistry*, **46**, 11263–11278.
30. Zou, Y., Shell, S.M., Utzat, C.D., Luo, C., Yang, Z., Geacintov, N.E. and Basu, A.K. (2003) Effects of DNA adduct structure and sequence context on strand opening of repair intermediates and incision by UvrABC nuclease. *Biochemistry*, **42**, 12654–12661.
31. Mekhovich, O., Tang, M. and Romano, L.J. (1998) Rate of incision of *N*-acetyl-2-aminofluorene and *N*-2-aminofluorene adducts by UvrABC nuclease is adduct- and sequence-specific: comparison of the rates of UvrABC nuclease incision and protein-DNA complex formation. *Biochemistry*, **37**, 571–579.
32. Jain, V., Hilton, B., Patnaik, S., Zou, Y., Chiarelli, M.P. and Cho, B.P. (2012) Conformational and thermodynamic properties modulate the nucleotide excision repair of 2-aminofluorene and 2-acetylaminofluorene dG adducts in the NarI sequence. *Nucleic Acids Res.*, **40**, 3939–3951.
33. Jain, N., Li, Y., Zhang, L., Meneni, S.R. and Cho, B.P. (2007) Probing the sequence effects on NarI-induced -2 frameshift mutagenesis by dynamic ¹⁹F NMR, UV, and CD spectroscopy. *Biochemistry*, **46**, 13310–13321.
34. Patnaik, S. and Cho, B.P. (2010) Structures of 2-acetylaminofluorene modified DNA revisited: Insight into conformational heterogeneity. *Chem. Res. Toxicol.*, **23**, 1650–1652.
35. O’Handley, S.F., Sanford, D.G., Xu, R., Lester, C.C., Hingerty, B.E., Broyde, S. and Krugh, T.R. (1993) Structural characterization of an *N*-acetyl-2-aminofluorene (AAF) modified DNA oligomer by NMR, energy minimization, and molecular dynamics. *Biochemistry*, **32**, 2481–2497.
36. Cho, B.P., Beland, F.A. and Marques, M.M. (1994) NMR structural studies of a 15-mer DNA duplex from a *ras* protooncogene modified with the carcinogen 2-aminofluorene: conformational heterogeneity. *Biochemistry*, **33**, 1373–1384.
37. Patel, D.J., Mao, B., Gu, Z., Hingerty, B.E., Gorin, A., Basu, A.K. and Broyde, S. (1998) Nuclear magnetic resonance solution structures of covalent aromatic amine-DNA adducts and their mutagenic relevance. *Chem. Res. Toxicol.*, **11**, 391–407.
38. Cho, B.P. (2004) Dynamic conformational heterogeneities of carcinogen-DNA adducts and their mutagenic relevance. *J. Environ. Sci. Health Pt. C Environ. Carcinogen. Ecotoxi. Rev.*, **C22**, 57–90.
39. Eckel, L.M. and Krugh, T.R. (1994) Structural characterization of two interchangeable conformations of a 2-aminofluorene-modified DNA oligomer by NMR and energy minimization. *Biochemistry*, **33**, 13611–13624.
40. Mao, B., Hingerty, B.E., Broyde, S. and Patel, D.J. (1998) Solution structure of the aminofluorene [AF]-external conformer of the *anti*-[AF]-C8-dG adduct opposite dC in a DNA duplex. *Biochemistry*, **37**, 95–106.
41. Mao, B., Hingerty, B.E., Broyde, S. and Patel, D.J. (1998) Solution structure of the aminofluorene [AF]-intercalated conformer of the *syn*-[AF]-C8-dG adduct opposite dC in a DNA duplex. *Biochemistry*, **37**, 81–94.
42. Eckel, L.M. and Krugh, T.R. (1994) 2-Aminofluorene modified DNA duplex exists in two interchangeable conformations. *Nat. Struct. Biol.*, **1**, 89–94.
43. Lukin, M. and de Los Santos, C. (2006) NMR structures of damaged DNA. *Chem. Rev.*, **106**, 607–686.
44. Stone, M.P., Huang, H., Brown, K.L. and Shanmugam, G. (2011) Chemistry and structural biology of DNA damage and biological consequences. *Chem. Biodivers.*, **8**, 1571–1615.
45. Zhou, L., Rajabjaded, M., Traficante, D.D. and Cho, B.P. (1997) Conformational heterogeneity of arylamine-modified DNA ¹⁹F NMR evidence. *J. Am. Chem. Soc.*, **119**, 5384–5389.
46. Norman, D., Abuaf, P., Hingerty, B.E., Live, D., Grunberger, D., Broyde, S. and Patel, D.J. (1989) NMR and computational characterization of the *N*-(deoxyguanosin-8-yl)aminofluorene adduct [(AF)G] opposite adenosine in DNA: (AF)G[*syn*].A[*anti*] pair formation and its pH dependence. *Biochemistry*, **28**, 7462–7476.
47. Jain, N., Meneni, S., Jain, V. and Cho, B.P. (2009) Influence of flanking sequence context on the conformational flexibility of aminofluorene-modified dG adduct in dA mismatch DNA duplexes. *Nucleic Acids Res.*, **37**, 1628–1637.
48. Abuaf, P., Hingerty, B.E., Broyde, S. and Grunberger, D. (1995) Solution conformation of the *N*-(deoxyguanosin-8-yl)aminofluorene adduct opposite deoxyinosine and deoxyguanosine in DNA by NMR and computational characterization. *Chem. Res. Toxicol.*, **8**, 369–378.
49. Wang, L. and Broyde, S. (2006) A new *anti* conformation for *N*-(deoxyguanosin-8-yl)-2-acetylaminofluorene (AAF-dG) allows Watson-Crick pairing in the *Sulfolobus solfataricus* P2 DNA polymerase IV (Dpo4). *Nucleic Acids Res.*, **34**, 785–795.
50. Shapiro, R., Hingerty, B.E. and Broyde, S. (1989) Minor-groove binding models for acetylaminofluorene modified DNA. *J. Biomol. Struct. Dyn.*, **7**, 493–513.
51. Burnouf, D., Koehl, P. and Fuchs, R.P. (1989) Single adduct mutagenesis: strong effect of the position of a single acetylaminofluorene adduct within a mutation hot spot. *Proc. Natl Acad. Sci. USA*, **86**, 4147–4151.

52. Fuchs,R.P., Schwartz,N. and Daune,M.P. (1981) Hot spots of frameshift mutations induced by the ultimate carcinogen *N*-acetoxy-*N*-2-acetylaminofluorene. *Nature*, **294**, 657–659.
53. Fuchs,R.P. and Fujii,S. (2007) Translesion synthesis in *Escherichia coli*: lessons from the *NarI* mutation hot spot. *DNA Repair (Amst.)*, **6**, 1032–1041.
54. Wang,F. and Yang,W. (2009) Structural insight into translesion synthesis by DNA Pol II. *Cell*, **139**, 1279–1289.
55. Janel-Bintz,R., Wagner,J., Haracska,L., Mah-Becherel,M.C., Bichara,M., Fuchs,R.P. and Cordonnier,A.M. (2012) Evidence for a rad18-independent frameshift mutagenesis pathway in human cell-free extracts. *PLoS One*, **7**, e36004.
56. Koehl,P., Valladier,P., Lefevre,J.F. and Fuchs,R.P. (1989) Strong structural effect of the position of a single acetylaminofluorene adduct within a mutation hot spot. *Nucleic Acids Res.*, **17**, 9531.
57. Kolbanovskiy,A., Kuzmin,V., Shastry,A., Kolbanovskaya,M., Chen,D., Chang,M., Bolton,J.L. and Geacintov,N.E. (2005) Base selectivity and effects of sequence and DNA secondary structure on the formation of covalent adducts derived from the equine estrogen metabolite 4-hydroxyequilenin. *Chem. Res. Toxicol.*, **18**, 1737–1747.
58. Kropachev,K., Kolbanovskii,M., Cai,Y., Rodriguez,F., Kolbanovskii,A., Liu,Y., Zhang,L., Amin,S., Patel,D., Broyde,S. et al. (2009) The sequence dependence of human nucleotide excision repair efficiencies of benzo[*a*]pyrene-derived DNA lesions: insights into the structural factors that favor dual incisions. *J. Mol. Biol.*, **386**, 1193–1203.
59. Case,D.A., Darden,T.A., Cheatham,T.E. III, Simmerling,C.L., Wang,J., Duke,R.E., Luo,R., Merz,K.M., Pearlman,D.A., Crowley,M. et al. (2006) *AMBER9*. University of California San Francisco, San Francisco, CA.
60. Case,D.A., Darden,T.A., Cheatham,T.E. III, Simmerling,C.L., Wang,J., Duke,R.E., Luo,R., Crowley,M., Walker,R.C., Zhang,W. et al. (2008) *AMBER10*. University of California San Francisco, San Francisco, CA.
61. Case,D.A., Pearlman,D.A., Caldwell,J.W., Cheatham,T.E. III, Wang,J., Ross,W.S., Simmerling,C.L., Darden,T.A., Merz,K.M., Stanton,R.V. et al. (2002) *AMBER7*. University of California San Francisco, San Francisco, CA.
62. Lavery,R., Moakher,M., Maddocks,J.H., Petkeviciute,D. and Zakrzewska,K. (2009) Conformational analysis of nucleic acids revisited: curves+. *Nucleic Acids Res.*, **37**, 5917–5929.
63. DeLano,W.L. (2002) The PyMol Molecular Graphic System, Version 1.3, Schrödinger, LLC.
64. Hess,M.T., Gunz,D., Luneva,N., Geacintov,N.E. and Naegeli,H. (1997) Base pair conformation-dependent excision of benzo[*a*]pyrene diol epoxide-guanine adducts by human nucleotide excision repair enzymes. *Mol. Cell. Biol.*, **17**, 7069–7076.
65. Mocquet,V., Kropachev,K., Kolbanovskiy,M., Kolbanovskiy,A., Tapias,A., Cai,Y., Broyde,S., Geacintov,N.E. and Egly,J.M. (2007) The human DNA repair factor XPC-HR23B distinguishes stereoisomeric benzo[*a*]pyrenyl-DNA lesions. *EMBO J.*, **26**, 2923–2932.
66. Jalal,S., Earley,J.N. and Turchi,J.J. (2011) DNA repair: from genome maintenance to biomarker and therapeutic target. *Clin. Cancer Res.*, **17**, 6973–6984.
67. Luijsterburg,M.S., von Bornstaedt,G., Gourdin,A.M., Politi,A.Z., Mone,M.J., Warmerdam,D.O., Goedhart,J., Vermeulen,W., van Driel,R. and Hofer,T. (2010) Stochastic and reversible assembly of a multiprotein DNA repair complex ensures accurate target site recognition and efficient repair. *J. Cell Bio.*, **189**, 445–463.
68. Koehl,P., Valladier,P., Lefevre,J.F. and Fuchs,R.P. (1989) Strong structural effect of the position of a single acetylaminofluorene adduct within a mutation hot spot. *Nucleic Acids Res.*, **17**, 9531–9541.
69. Cai,Y., Geacintov,N.E. and Broyde,S. (2012) Nucleotide excision repair efficiencies of bulky carcinogen-DNA adducts are governed by a balance between stabilizing and destabilizing interactions. *Biochemistry*, **51**, 1486–1499.
70. Cai,Y., Kropachev,K., Kobanovskiy,M., Kolbanovskiy,A., Broyde,S., Patel,D.J. and Geacintov,N.E. (2010) Recognition and removal of bulky DNA lesions by the DNA nucleotide excision repair system. In: Geacintov,N.E. and Broyde,S. (eds), *The Chemical Biology of DNA Damage*. Wiley-VCH, Weinheim, Germany, pp. 261–298.
71. Reeves,D.A., Mu,H., Kropachev,K., Cai,Y., Ding,S., Kolbanovskiy,A., Kolbanovskiy,M., Chen,Y., Krzeminski,J., Amin,S. et al. (2011) Resistance of bulky DNA lesions to nucleotide excision repair can result from extensive aromatic lesion-base stacking interactions. *Nucleic Acids Res.*, **39**, 8752–8764.
72. Hoare,S., Zou,Y., Purohit,V., Krishnasamy,R., Skorvaga,M., Van Houten,B., Geacintov,N.E. and Basu,A.K. (2000) Differential incision of bulky carcinogen-DNA adducts by the UvrABC nuclease: comparison of incision rates and the interactions of Uvr subunits with lesions of different structures. *Biochemistry*, **39**, 12252–12261.
73. Ding,S., Kropachev,K., Cai,Y., Kolbanovskiy,M., Durandina,S.A., Liu,Z., Shafirovich,V., Broyde,S. and Geacintov,N.E. (2011) Structural, energetic and dynamic properties of guanine(C8)-thymine(N3) cross-links in DNA provide insights on susceptibility to nucleotide excision repair. *Nucleic Acids Res.*, **40**, 2506–2517.
74. Cai,Y., Ding,S., Geacintov,N.E. and Broyde,S. (2011) Intercalative conformations of the 14R (+)- and 14S (-)-*trans-anti*-DB[*a*,*l*]P-*N*⁶-dA adducts: molecular modeling and MD simulations. *Chem. Res. Toxicol.*, **24**, 522–531.
75. Neidle,S., Kuroda,R., Broyde,S., Hingerty,B.E., Levine,R.A., Miller,D.W. and Evans,F.E. (1984) Studies on the conformation and dynamics of the C8-substituted guanine adduct of the carcinogen acetylaminofluorene; model for a possible Z-DNA modified structure. *Nucleic Acids Res.*, **12**, 8219–8233.
76. Dutta,S., Li,Y., Johnson,D., Dzantiev,L., Richardson,C.C., Romano,L.J. and Ellenberger,T. (2004) Crystal structures of 2-acetylaminofluorene and 2-aminofluorene in complex with T7 DNA polymerase reveal mechanisms of mutagenesis. *Proc. Natl Acad. Sci. USA*, **101**, 16186–16191.
77. Rechkooblit,O., Kolbanovskiy,A., Malinina,L., Geacintov,N.E., Broyde,S. and Patel,D.J. (2010) Mechanism of error-free and semitargeted mutagenic bypass of an aromatic amine lesion by Y-family polymerase Dpo4. *Nat. Struct. Mol. Biol.*, **17**, 379–388.
78. Neidle,S., Pearl,L.H., Herzyk,P. and Berman,H.M. (1988) A molecular model for proflavine-DNA intercalation. *Nucleic Acids Res.*, **16**, 8999–9016.
79. Li,S., Cooper,V.R., Thonhauser,T., Lundqvist,B.I. and Langreth,D.C. (2009) Stacking interactions and DNA intercalation. *J. Phys. Chem. B*, **113**, 11166–11172.
80. Liu,Y., Reeves,D., Kropachev,K., Cai,Y., Ding,S., Kolbanovskiy,M., Kolbanovskiy,A., Bolton,J.L., Broyde,S., Van Houten,B. et al. (2011) Probing for DNA damage with beta-hairpins: similarities in incision efficiencies of bulky DNA adducts by prokaryotic and human nucleotide excision repair systems in vitro. *DNA Repair (Amst.)*, **10**, 684–696.
81. Tan,X., Suzuki,N., Grollman,A.P. and Shibusaki,S. (2002) Mutagenic events in *Escherichia coli* and mammalian cells generated in response to acetylaminofluorene-derived DNA adducts positioned in the *Nar I* restriction enzyme site. *Biochemistry*, **41**, 14255–14262.
82. Cai,Y., Patel,D.J., Geacintov,N.E. and Broyde,S. (2009) Differential nucleotide excision repair susceptibility of bulky DNA adducts in different sequence contexts: hierarchies of recognition signals. *J. Mol. Biol.*, **385**, 30–44.
83. Cornell,W.D., Cieplak,P., Bayly,C.I., Gould,I.R., Merz,K.M., Ferguson,D.M., Spellmeyer,D.C., Fox,T., Caldwell,J.W. and Kollman,P.A. (1995) A second generation force field for the simulation of proteins, nucleic acids, and organic molecules. *J. Am. Chem. Soc.*, **117**, 5179–5197.
84. Wang,J.M., Cieplak,P. and Kollman,P.A. (2000) How well does a restrained electrostatic potential (RESP) model perform in calculating conformational energies of organic and biological molecules? *J. Comput. Chem.*, **21**, 1049–1074.
85. Pérez,A., Marchán,I., Svozil,D., Sponek,J., Cheatham,T.E. 3rd, Loughton,C.A. and Orozco,M. (2007) Refinement of the AMBER force field for nucleic acids: improving the description of α/γ conformers. *Biophys. J.*, **92**, 3817–3829.

86. Wang, J.M., Wolf, R.M., Caldwell, J.W., Kollman, P.A. and Case, D.A. (2004) Development and testing of a general amber force field. *J. Comput. Chem.*, **25**, 1157–1174.
87. Cieplak, P., Cornell, W.D., Bayly, C. and Kollman, P.A. (1995) Application of the multimolecule and multiconformational resp methodology to biopolymers—charge derivation for DNA, RNA and proteins. *J. Comput. Chem.*, **16**, 1357–1377.
88. Frisch, M.J., Trucks, G.W., Schlegel, H.B., Scuseria, G.E., Robb, M.A., Cheeseman, J.R., Montgomery, J.A. Jr, Vreven, T., Kudin, K.N., Burant, J.C. *et al.* (2004) *Gaussian 03, Revision B.*, 5th edn. Gaussian, Inc., Wallingford, CT.
89. Bayly, C.I., Cieplak, P., Cornell, W.D. and Kollman, P.A. (1993) A well-behaved electrostatic potential based method using charge restraints for deriving atomic charges—the RESP model. *J. Phys. Chem.*, **97**, 10269–10280.
90. Berendsen, H.J.C., Postma, J.P.M., Vangunsteren, W.F., Dinola, A. and Haak, J.R. (1984) Molecular-dynamics with coupling to an external bath. *J. Chem. Phys.*, **81**, 3684–3690.
91. Flyvbjerg, H. and Petersen, H.G. (1989) Error-estimates on averages of correlated data. *J. Chem. Phys.*, **91**, 461–466.
92. Yang, W., Bitetti-Putzer, R. and Karplus, M. (2004) Free energy simulations: use of reverse cumulative averaging to determine the equilibrated region and the time required for convergence. *J. Chem. Phys.*, **120**, 2618–2628.
93. Saenger, W. (1984) *Principles of Nucleic Acid Structure*. Springer, New York.
94. Altona, C. and Sundaralingam, M. (1972) Conformational analysis of the sugar ring in nucleosides and nucleotides. A new description using the concept of pseudorotation. *J. Am. Chem. Soc.*, **94**, 8205–8212.
95. Cho, B.P. and Zhou, L. (1999) Probing the conformational heterogeneity of the acetylaminofluorene-modified 2'-deoxyguanosine and DNA by ¹⁹F NMR spectroscopy. *Biochemistry*, **38**, 7572–7583.
96. Evans, F.E., Miller, D.W. and Levine, R.A. (1984) Conformation and dynamics of the 8-substituted deoxyguanosine 5'-monophosphate adduct of the carcinogen 2-(acetylamino)fluorene. *J. Am. Chem. Soc.*, **106**, 396–401.
97. Johnson, R.C., Stella, S. and Heiss, J.K. (2008) Bending and compaction of DNA by proteins. In: Rice, P.A. and Correll, C.C. (eds), *Protein-Nucleic Acid Interactions: Structural Biology*. The Royal Society of Chemistry, Cambridge, pp. 176–220.